Article

A Synergistic Strategy through Microstructuring and Graphene Doping for High-Output Silk Fibroin-Based Triboelectric Nanogenerators toward Self-Powered Systems

Baizheng Zhu [1,†], Shiqi Zhang [1,†], Aoxiong He [1], Meng Sun [1], Qiaolin Fan [1], Zhonghua Ni [1,2], Xiao Li [1,2,]* and Tao Hu [1,2,]*

[1] School of Mechanical Engineering, Jiangsu Key Laboratory for Design and Manufacturing of Precision Medicine Equipment, Southeast University, Nanjing 211189, China
[2] Advanced Ocean Institute of Southeast University, Nantong 226010, China
*   Correspondence: lx2016@seu.edu.cn (X.L.); hutao@seu.edu.cn (T.H.)
†   These authors contributed equally to this work.

Abstract: The pursuit of sustainable and high-performance energy harvesters has driven growing interest in triboelectric nanogenerators (TENGs), yet challenges remain in balancing output enhancement, material biocompatibility, and fabrication simplicity. Herein, we report a high-efficiency silk fibroin–PTFE TENG engineered through finite-element simulations, structure optimization and graphene-assisted conductivity modulation. Biocompatible silk fibroin films were microstructured with well-defined pyramid and arch arrays in different microstructure densities, significantly increasing surface charge density and contact area. The optimized TENG with micro-arch silk fibroin achieved a peak-to-peak open-circuit voltage of 224 V and a short-circuit current of 12.74 μA, corresponding to over sixfold and threefold improvements, respectively, over TENGs without microstructure. Moreover, reduced graphene oxide (rGO) incorporation further enhanced the output performance of the TENG, with the peak-to-peak open-circuit voltage and short-circuit current reaching 288 V and 20 μA, respectively, resulting in additional improvements of 28.57% and 56.99%. Leveraging these advances, a 3 × 3 self-powered digital recognition array based on the silk fibroin/graphene-PTFE TENG demonstrated a recognition accuracy of 96.05%, validating its applicability in intelligent human-machine interfaces. This work presents a scalable and environmentally benign route to fabricating flexible TENGs with superior electrical performance and robust operational stability, bridging sustainable materials and advanced self-powered electronics.

Keywords: TENG; silk fibroin; microstructure; graphene; PTFE; self-powered system

1. Introduction

Triboelectric nanogenerators (TENGs) have emerged as a promising technology for scavenging mechanical energy from ambient environment [1]. Since the pioneering work by Zhonglin Wang's research group, TENGs offer distinct advantages including broad material selectivity, low-cost fabrication, and high efficiency at harvesting low-frequency and irregular mechanical energy, compared to conventional electromagnetic generators [2–4]. These

metrics make TENGs particularly suitable in self-powered electronics, human-machine interfaces, and health monitoring systems. The versatility of TENGs is largely underpinned by the extensive selection of triboelectric materials, among which polymers play a dominant role due to their excellent flexibility, ease of processing, and superior surface properties [5–8].

Polymeric materials, such as polydimethylsiloxane (PDMS), polytetrafluoroethylene (PTFE) and polyimide (PI), present significant advantages over conventional metallic and semiconductor substrates, including superior flexibility, conformability, and durability [5]. In particular, PTFE demonstrates a distinctive combination of exceptional chemical inertness, minimal interfacial friction, and outstanding triboelectric performance, making it one of the most effective tribo-negative materials [7]. However, conventional TENGs primarily rely on synthetic polymers, which offer high triboelectric performance but lack biodegradability and may pose environmental concerns [9,10]. These limitations have consequently redirected research efforts toward exploring sustainable alternatives derived from natural polymer systems that combine triboelectric functionality with ecological viability [11,12]. Under this circumstance, silkworm silk fibroin has gained attention as a representative natural biopolymer due to its excellent biocompatibility, biodegradability, and promising dielectric properties, offering a sustainable pathway for scalable manufacturing of TENG devices [11].
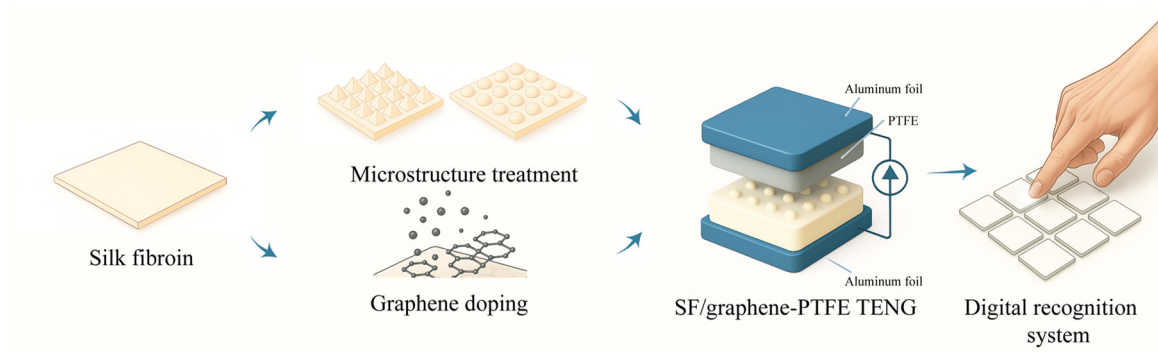
Enhanced TENG outputs enable broader application viability. Numerous strategies have emerged to improve TENG performance, with increasing surface charge density of triboelectric layers standing out as an effective approach. Compared with the pursuit of new configurations, improving the output performance through surface microstructure modification is relatively straightforward and cost-effective [13,14]. The introduction of micro- and nano-structures on triboelectric films is a rational approach, as it directly increases the effective contact area for charge generation [15,16]. The size, shape, and hierarchy of these structures critically influence the output [17,18]. For instance, micro-patterned PDMS surfaces and various porous or fibrous structures have been shown to significantly boost voltage and current outputs, with different structures leading to enhancements of several hundred percent compared to flat films [16,19–21]. Methods to create these microstructures, such as etching (e.g., laser, plasma) and replication (e.g., imprint lithography), are effective but can be costly, highlighting the need for cost-effective methods like mold imprinting [22–24].

The composition of dielectric layer materials is also crucial for enhancing the performance of TENGs. Two-dimensional (2D) nanomaterials, known for their excellent electronic properties, mechanical flexibility, transparency, and high specific surface area, are widely used in TENG dielectric layers [25–27]. Materials such as transition metal dichalcogenides (TMDs) [28], layered covalent organic frameworks (COFs) [29], layered metal-organic frameworks (MOFs) [30], MXenes [31], graphene [32], and graphene oxide (GO) [33] not only reduce the internal impedance of TENGs and increase the amount of induced charge, but their ultra-high specific surface area also enables longer retention of triboelectric charges, making it feasible to fabricate very thin devices within stacked structures. Among various materials, carbon-based nanomaterials are particularly prominent. Multi-walled carbon nanotubes (MWCNTs) have been effectively incorporated into polymers like PDMS and nylon to enhance dielectric constant and triboelectric output [27,34]. Graphene and its derivatives offer distinct advantages due to their two-dimensional geometry and ultra-high specific surface area, which benefits charge retention and interface engineering [35,36]. Common graphene synthesis methodologies include mechanical exfoliation, chemical vapor deposition (CVD), oxidation-reduction processes, liquid-phase exfoliation, and electrochemical methods [37–40]. Among these, the oxidation-reduction approach remains the most widely employed technique.

This study introduces a silk fibroin–PTFE TENG that combines the eco-friendly and biocompatible nature of silk fibroin with the excellent triboelectric properties of PTFE. Through micro-pyramid and micro-arch surface mold imprinting, the charge transfer efficiency is substantially improved without complex fabrication steps. The graphene-doped silk fibroin composite further enhances conductivity and mechanical properties while preserving biodegradability. Importantly, the integration of these materials into a self-powered digital recognition system demonstrates a practical, low-cost, and environmentally sustainable solution for human–machine interfaces.

2. Results and Discussion

Scheme 1 illustrates the fabrication and application process of the dual-optimized silk fibroin (SF)/graphene-PTFE TENG. SF films undergo microstructure patterning and graphene doping, while PTFE layers are roughened by sandpaper treatment. The assembled SF/graphene-PTFE TENG exhibits enhanced electrical output and is further applied in a self-powered digital recognition system.

Scheme 1. Schematic illustration of the fabrication and application process of the dual-optimized SF/graphene-PTFE TENG.

2.1. Characterization of SF Films and SF/Graphene Films

The fabrication process yielded a transparent, pale yellow fibroin film with uniform thickness, as shown in Figure 1a–c. The surface and internal morphology of the SF films were observed using a scanning electron microscope (SEM). As shown in Figure S1a, the surface of the SF film is smooth and flat, with only a few micrometer-sized impurities. Figure 1d shows the cross-section of the SF film, which was formed by stretching and breaking after uniform tension was applied at both ends of the SF film. The figure illustrates that the thickness of the film is approximately 550 μm, with raised wave patterns and textures. This texture is the internal fiber structure of the SF film, as it was subjected to strong tensile force during the stretching process, resulting in a relatively obvious wave-like texture.

Figure 1. (**a**–**c**) Photographs of a highly transparent, flexible and skin-friendly SF film; (**d**) SEM image of the interior of the SF film; (**e**) SEM image of the SF/graphene film; (**f**) X-ray diffraction test result of SF; (**g**) Raman spectroscopy of SF/graphene film and SF film; (**h**) Tensile stress-strain curves of the SF film and SF/graphene films; (**i**) Degradation test of silk protein films using deionized water for 45 days.

X-ray diffraction (XRD) is an analytical technique that utilizes the interaction between incident X-rays and the crystalline lattice of a material to generate diffraction patterns, from which critical structural parameters can be derived. In the case of SF, the predominant crystalline phases are identified as Silk I and Silk II, with trace amounts of the unstable Silk III structure occasionally observed at the air/water interface [11,41,42]. Structurally, Silk I consists of amorphous domains containing α-helical configurations and other non-β-sheet conformations, whereas Silk II is characterized by well-ordered crystalline regions featuring antiparallel β-sheet arrangements. As evidenced by the XRD spectrum presented in Figure 1f, the diffraction profile shows a prominent peak at 20.5°, corresponding to the crystalline Silk II phase, while a weaker shoulder at 23.69° is attributable to the Silk I structure. The relative intensity of these peaks provides important structural insights: the significantly stronger diffraction signal from the Silk II phase indicates both higher crystallinity and greater molecular ordering compared to the Silk I structure. It should be noted that the XRD measurement range was limited to $2\theta = 40°$ because the characteristic diffraction peaks for the β-sheet crystals in SF, which contain all relevant structural information, are located within this low-angle region. This range is therefore sufficient to determine crystallinity, crystal size, and molecular orientation corresponding to SF materials. These observations confirm that the Silk II conformation represents the dominant and thermodynamically stable crystalline form within the SF films.

Figure 1e demonstrates the layered three-dimensional porous morphology observed on the surface of the SF/graphene composite film, which is attributed to the structural integration of reduced graphene oxide (rGO) within the SF matrix. The graphene nanosheets are uniformly dispersed in the SF substrate, with evident structural overlapping between adjacent graphene layers. This characteristic stacking configuration provides conclusive evidence for the successful fabrication of the SF/graphene composite film.

To further verify the successful incorporation of rGO into SF films and to determine the number of graphene layers, Raman spectroscopy was performed on both pure SF films and SF/graphene composite films, as shown in Figure 1g. The composite films exhibited characteristic D and G bands at 1341 cm^{-1} and 1596 cm^{-1}, respectively, while the pure SF film showed no significant peaks, confirming the successful integration of rGO. The D band is related to structural defects, and the G band corresponds to the in-plane vibration of sp^2-hybridized carbon atoms. The intensity ratio I_D/I_G was calculated as 1.048, indicating the presence of a certain amount disordered structures in rGO, resulting from increased sp^2 domains during in-situ reduction or unrepaired defects after the removal of oxygen-containing groups. The 2D band, a unique marker of graphene structure, was observed at 2935 cm^{-1}. The intensity ratio I_{2D}/I_D was determined to be 1.018, which falls within the range between 1 and 2, indicating that rGO is few-layer structure [43].

The mechanical properties of the gel film, such as its elastic modulus and elongation at break, are critical parameters. For subsequent applications in wearable devices, the film must possess adequate flexibility and extensibility. These properties are essential to ensure conformability to the contours and movements of various body parts. Figure S1b shows the cross-sectional morphology of the SF film after tensile fracture. Compared to the wave-like pattern observed in the knife-cut cross-section via SEM in Figure 1d, the tensile-fractured section exhibits a more prominently raised wave pattern with clearer texture. This phenomenon is attributed to the stronger tensile stress endured by the internal fibrous structure of the film during stretching, leading to more pronounced deformation and texture evolution. Similarly, Figure S1c reveals a distinct corrugated pattern on the fracture surface of the composite film after tensile failure. Figure 1h illustrates the tensile stress-strain curves of the SF and SF/graphene films. As for SF films, fracture occurs when the tensile deformation reaches a critical point of 66.63%. Prior to fracture, the stress-strain curve demonstrates a strong linear relationship, indicating excellent mechanical flexibility of the film during the tensile process. This property enables effective conformability to curved areas such as human joints, thereby providing a reliable basis for the accurate monitoring of movement postures. As for SF/graphene films, the elongation at break of the SF/graphene composite film reached 99.95%, representing a 50.01% increase compared to that of the SF film. These results indicate that the incorporation of rGO significantly enhances the tensile performance of SF, imparting excellent flexibility to the composite film.

Degradable TENGs break down into harmless fragments, reducing environmental impact, resource consumption, and operational costs, making them eco-friendly and cost-effective for future use. SF films, with their distinct Silk I and Silk II conformations, show degradation rates influenced by β-sheet content. Lower crystallinity accelerates degradation, enabling programmable biodegradation from hours to years. This structural plasticity enhances the processability and versatility of SF devices, broadening their potential applications. To explore the biodegradability of SF films, degradation test of SF films was conducted in deionized water to simulate their decomposition in real-world environments. As illustrated in Figure 1i, within 3 days, the films swelled but remained transparent and intact. By day 15, optical transparency and dimensions reduced. By day 30, a cloud-like morphology formed, and by day 45, the films degraded into nearly invisible particles. These experimental results provide compelling evidence for the exceptional degradability of SF films under certain aqueous conditions.

Similarly, a biodegradability test was conducted on the SF/graphene composite films, using deionized water, as illustrated in Figure S2. This test showed slow degradation due to the absence of natural decomposers. Films remained largely unchanged in the first 14 days, began lightening and curling by week 4, fragmented by day 42, and fully degraded by day 63. The uniform distribution of rGO within the SF matrix provides enhanced structural support, which effectively impedes the penetration of water molecules. This reinforcement increases the structural stability of the SF/graphene composite film, thereby decelerating its degradation rate. The degradation experiment confirms the biodegradable nature of the composite, demonstrating its environmental friendliness and potential as a sustainable material.

2.2. The Optimization of the Output Performance of SF-PTFE TENG by Surface Microstructure

Systematic investigation of TENG performance revealed that SF films with microstructures demonstrated optimal enhancement in electrical output characteristics. To explore the influence of surface microstructure on the performance of TENG, two structures, micro-pyramid and micro-arch, were selected for comparison and selection among different structures. As for the mold, the base dimensions of each micro-pyramid structure are 1 mm × 1 mm, the base diameter of each micro-arch structure is 1 mm, and the height of both types of microstructures is 0.5 mm. Furthermore, for the same structure, different structural densities are used to select the optimal structural density, thereby obtaining the best structure within the feasible range of using molds for production.

Two types of microstructures have been created on the surface of 50 mm × 50 mm SF films, namely pyramids and arches. The molds, physical samples and structural diagrams of these two types are shown in the Figure 2a. SEM analysis (Figure 2b,c) illustrated distinct microstructural features within the 1×1 mm^2 observation area. The micro-pyramid architectures exhibited a slight structural collapse, manifesting as concave pit-like formations while maintaining seamless integration with the substrate at the base interface, with a height of 498 μm. It is speculated that during the heating process of the SF solution as it solidifies into a gel-like state, the residual air in the solution accumulates to form bubbles, which causes the microstructure of the pyramid body to collapse during the release process. Furthermore, as shown in Figure 2d,e, a single arch structure can be seen clearly. The overall dimensions of the arch are 1×1 mm^2, with a height of 501 μm. While the arch-shaped structure appears largely intact, local depressions of varying degrees are present. Notably, the terminus of the structure is smoothly integrated with the substrate, suggesting a strong bond between the microstructure and the substrate. The arch-shaped microstructure exhibits greater completeness in comparison to the pyramid microstructure, with a reduced collapsed area, which is hypothesized to result from a less concentrated stress distribution on the arch body.
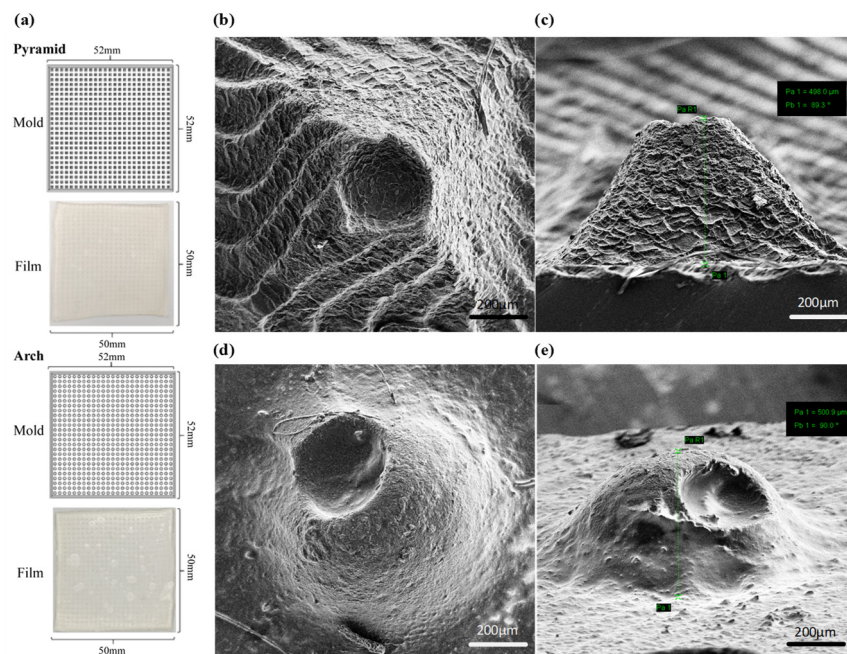

Figure 2. (**a**) Schematic diagrams of the SF films and the corresponding molds with pyramid and arch microstructures at a density of 25 units/cm^2; (**b**) Individual pyramidal microstructure on the surface of SF films under SEM; (**c**) The side view of the pyramidal microstructure on the surface of SF films under SEM; (**d**) Individual arch-shaped microstructure on the surface of SF films under SEM; (**e**) The side view of the arch-shaped microstructure on the surface of SF films under SEM.

The working principle of the SF-PTFE TENG in one cycle is shown in Figure 3a. TENG operates on the principle of the triboelectric effect and electrostatic induction, where electron transfer between two materials during contact creates opposite charges, and their subsequent separation generates a potential difference that drives a current. The detailed working principle can be found in Supplementary Materials S1.
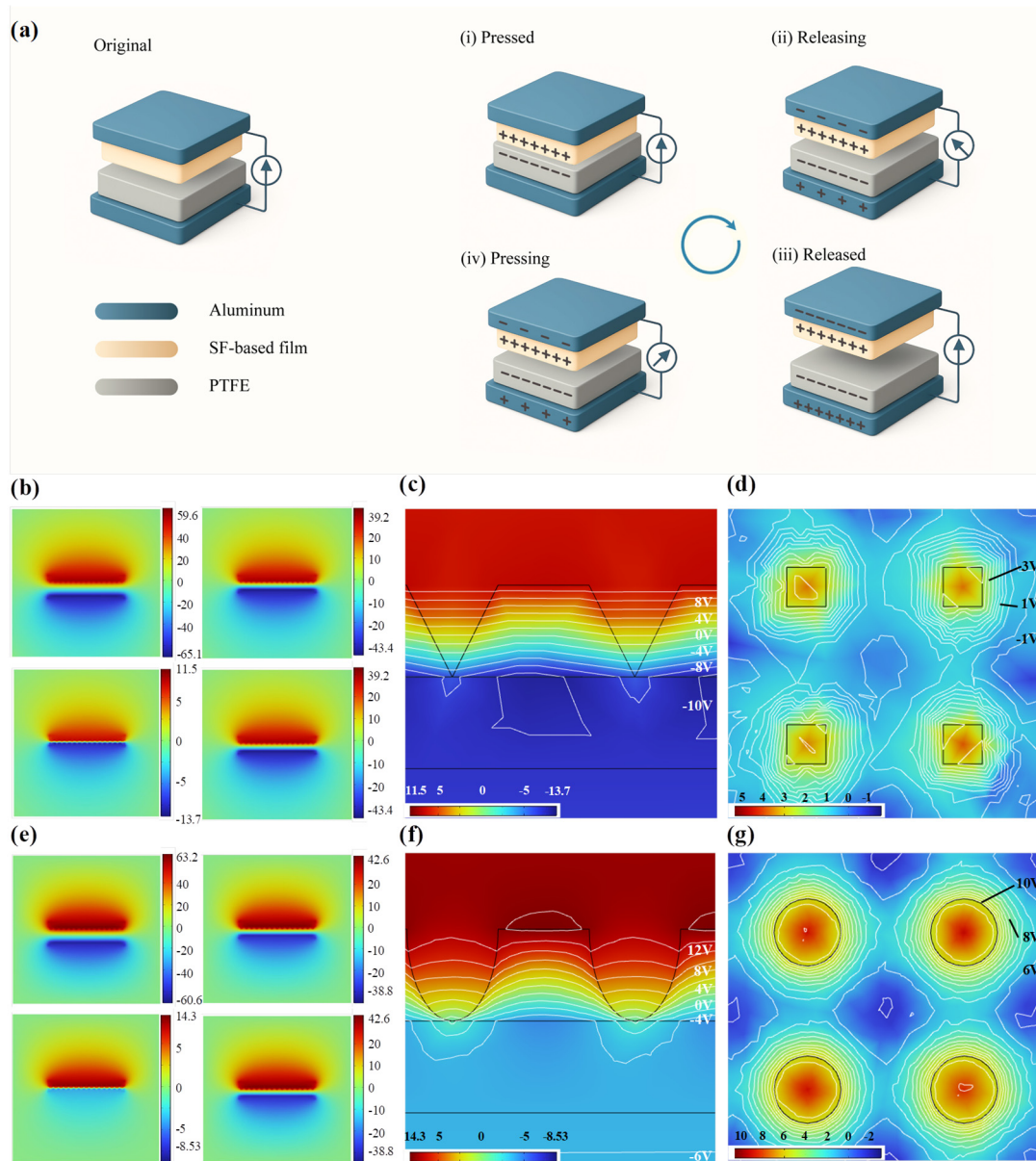

Figure 3. (**a**) The working principle of SF-PTFE TENG in a single cycle; (**b**) Electric potential distribution of the TENGs with micro-pyramid; (**c**) Sectional view and (**d**) Top view of potential contours at 0.5 mm height of pyramids obtained from simulation; (**e**) Electric potential distribution of the TENG with micro-arch; (**f**) Sectional view and (**g**) Top view of potential contours at 0.5mm height of arches obtained from simulation.

To simulate the potential distribution of SF-PTFE TENGs with different surface microstructures during operation, finite element analysis was performed using COMSOL. For flat surfaces (Figure S3), the potential distribution appears more uniform across the contact area. Figure 3b,e demonstrate that the potential distributions of the pyramid and arch structures exhibit similarities to those of the flat structures. However, in the case of the pyramid and arch structures, there are notable differences in the potential distribution compared to the flat surface. From a quantitative analysis standpoint, as presented in Figure S4, the TENGs with surface microstructures consistently exhibit higher potentials compared to the TENGs without surface microstructures. Additionally, the arch structures exhibit higher maximum potentials during both the contact and separation phases, and reach their peak advantage in the contact phase. The potential contours in sectional views (Figure 3c,f) indicate areas of higher concentration around the sharp tips or curves, suggesting higher surface charge densities at these points. This can be associated with the enhanced triboelectric effects due to the local increase in contact force at the tips of these

structures, which could lead to higher energy generation during the contact process. The top views (Figure 3d,g) reveal that these microstructures concentrate and redistribute the electric field especially around every single pyramid and arch, leading to improved performance in energy harvesting compared to flat surfaces. Furthermore, the theoretical surface contact areas of the two microstructural arrays employed in this study were calculated. Both the micro-pyramid and micro-arch arrays are arranged in a 15 × 15 layout on a 50 mm × 50 mm film surface. The total surface area was determined by calculating the surface area of a single microstructure (using geometric derivation for the micro-pyramid and surface integration for the micro-arch) and then multiplying by the total number of structures in the array. The analysis of the theoretical surface contact area reveals that the surface areas of the micro-pyramid and micro-arch are approximately 503.1 mm^2 and 603.9 mm^2, respectively. This difference may partially account for the superior performance observed in the micro-arch TENGs.

For experimental validation under practical working conditions, an external driving force was applied to the TENG using a linear motor operating at a frequency of approximately 2 Hz. For the purpose of minimizing edge-induced errors in the film demolding process and achieving a compact and lightweight design, the films were all cut to an area of 30mm × 30mm from the central region. As illustrated in Figure 4a–d, numbers ranging from 0 to 25 represent different microstructure densities. The positive voltage peak of the original TENG without any microstructures ranged between 16 to 20 V. The maximum peak-to-peak values for open-circuit voltage and short-circuit current were recorded as 33.06 V and 2.9 µA, respectively. These results are consistent with the performance range of conventional flexible TENGs, which often face limitations in output for practical biomedical applications without structural optimization. This underscores the necessity for performance enhancement strategies, such as surface microtexturing explored here or scalable fabrication methods like spray-coating [44].

The incorporation of micro-pyramidal structures into the silk fibroin films enhanced the TENG's electrical output. As shown in Figure 4a, the positive voltage and current peak at 52.31 V and 7.32 µA, respectively. This enhancement can be attributed to the increased effective contact area and local pressure concentration provided by the microstructures, which intensify contact electrification—a principle similarly observed in TENGs utilizing micropillar arrays to amplify energy harvesting from subtle mechanical stimuli [44]. Notably, the open-circuit voltage amplitude grew significantly with increasing micro-pyramid density, and the short-circuit current amplitude showed a consistent upward trend across the four density variations. At a density of 25 units/cm^2, the peak-to-peak open-circuit voltage and short-circuit current reached approximately 86 V and 14 µA, representing improvements exceeding 160.1% and 382% over the non-microstructured TENG.

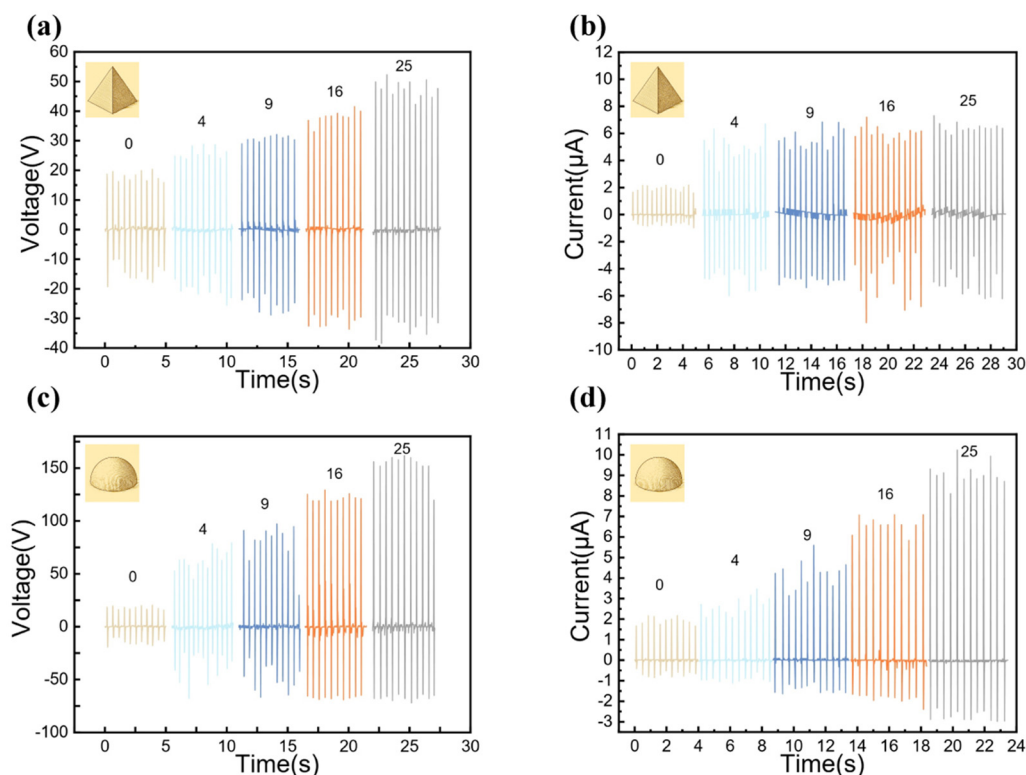**Figure 4.** (**a**) Open-circuit voltage and (**b**) Short-circuit current diagrams of TENGs with micro-pyramid SF surfaces; (**c**) Open-circuit voltage and (**d**) Short-circuit current diagrams of TENGs with micro-arch SF surfaces.

Furthermore, when compared to devices with micro-pyramidal structures, TENGs featuring arch-shaped microstructures exhibited more pronounced enhancement in open-circuit voltage peaks. Specifically, the maximum peak-to-peak open-circuit voltage reached 224 V for the mold with 25 units/cm^2 density, representing over 600% increase over the values of non-microstructured TENG and a 181.4% improvement compared to micro-pyramidal TENG. The superior performance stems from the distinct charge generation and retention dynamics facilitated by the arch geometry. The curved surface promotes more efficient charge accumulation and localization during the contact-separation cycle, resulting in a higher surface charge density, analogous to the function of biocompatible, skin-conformal designs aimed at maximizing charge transfer efficiency while maintaining flexibility. The peak-to-peak short-circuit current was 12.74 μA, merely 91% of the value of micro-pyramid. It is speculated that the sharpness of the pyramid tips can enhance the transfer of charges from the surface to the external circuit, increasing the overall current generation efficiency, causing higher short-circuit current of micro-pyramidal TENG.

In addition, for a more intuitive systematic assessment, Figure S5 presents a bar chart comparing the maximum peak-to-peak outputs of each structure at the same density of 25 units/cm^2. Comparative analysis confirms the critical role of surface microtexturing in optimizing TENG output, with the micro-arch structure achieving a sixfold increase in voltage, aligning with the field's ongoing efforts to develop high-performance, self-powered medical devices [44,45]. Thus, due to the substantial increase in peak-to-peak open-circuit voltage and decent improvement in peak-to-peak short-circuit current, subsequent experiments were conducted using the arch-shaped TENGs with a microstructure density of 25 units/cm^2. Furthermore, a durability test at a frequency of 2 Hz was conducted on the chosen SF-PTFE TENG to confirm its operational stability under continuous working conditions. As illustrated in Figure S6a, the device demonstrated consistent and stable output throughout the 400-s test, indicating excellent reliability.

2.3. The Optimization of the Output Performance of SF-PTFE TENG by Graphene Doping

In the fabrication of SF/graphene composite films, the concentration of rGO constitutes a pivotal variable, as it directly governs the output performance of the TENGs derived from these films. To systematically investigate the effect of rGO concentration, five SF solutions were prepared with rGO loadings ranging from 0 to 1 mg, incremented in steps of 0.25 mg. These mixtures were subsequently solidified into composite films with an arch structure density of 25 units/cm^2. TENGs were then assembled using these films against PTFE films with identical surface properties under the working conditions of a 2 Hz operating frequency and a contact area of 9 cm^2. The resulting TENGs were integrated into a measurement circuit, and their output performance was characterized, as summarized in Figure 5a,b.

The experimental data indicate a positive correlation between increasing rGO concentration and the enhancement of both open-circuit voltage and short-circuit current. Peak-to-peak values reached maxima of 288 V and 20 μA, respectively. At an rGO concentration of 1 mg, the peak-to-peak open-circuit voltage and short-circuit current increased by approximately 28.57% and 56.99%, respectively, compared to the undoped sample. This improvement can be attributed to the formation of conductive pathways by rGO sheets within the silk fibroin matrix, which effectively reduces the surface resistance and facilitates charge transfer during triboelectrification [46]. A notable observation was that the negative peak of the short-circuit current nearly doubled as the graphene content increased from 0.25 mg to 0.5 mg. This behavior is characteristic of percolation threshold phenomena in conductor-insulator composites, where the formation of a continuous conductive network dramatically improves charge transport capabilities, consistent with observations in other nanofiller-doped TENG systems [47]. However, beyond the optimal concentration range, specifically above 0.75 mg, the material properties exhibited significant deterioration. The homogeneous dispersion of rGO in the SF matrix became increasingly challenging, leading to nanoparticle aggregation and precipitation. This phase separation resulted in heterogeneous film morphology and compromised structural integrity [48]. Furthermore, the excessive rGO loading induced alterations in the secondary structure of SF and substantially reduced optical transmittance, thereby limiting potential applications where transparency or biocompatibility are essential. Based on the comprehensive evaluation of electrical output and material properties, an rGO concentration of 0.5 mg was identified as optimal for achieving balanced performance in SF composite films, providing the foundation for subsequent investigations.

Moreover, to evaluate the impact of operating frequency on the SF/graphene-PTFE TENG's performance in practical low-frequency scenarios, contact-separation tests were conducted at varying frequencies between 1 Hz to 5 Hz. Results indicated that both open-circuit voltage and short-circuit current increased with frequency, as illustrated in Figure 5c,d. At 5 Hz, the short-circuit current peak-to-peak value was 3.06 times higher than at 1 Hz. This behavior can be explained by established TENG models, which indicate that higher frequencies reduce the time available for charge recombination between cycles, thereby promoting more effective surface charge

separation and accumulation [49]. The observed enhancement is further amplified by the incorporation of rGO, which improves charge conduction within the composite [46]. This study focuses on energy harvesting from low-frequency human motion, generally a much lower frequency within 5Hz compared to other scenarios, such as machine vibration or other environmental vibration energy (typically 1 Hz to 50 Hz) [50]. Therefore, the frequency range between 1 Hz to 5 Hz aligns with this practical application scenario. To evaluate the long-term stability of the SF/graphene-PTFE TENG with a concentration of 0.5 mg, an extended durability test was performed at 2 Hz. The results, presented in Figure S6b, show that the TENG remarkably maintained a consistent and stable output over a period of 400 s, thereby verifying its robustness for sustained operation.
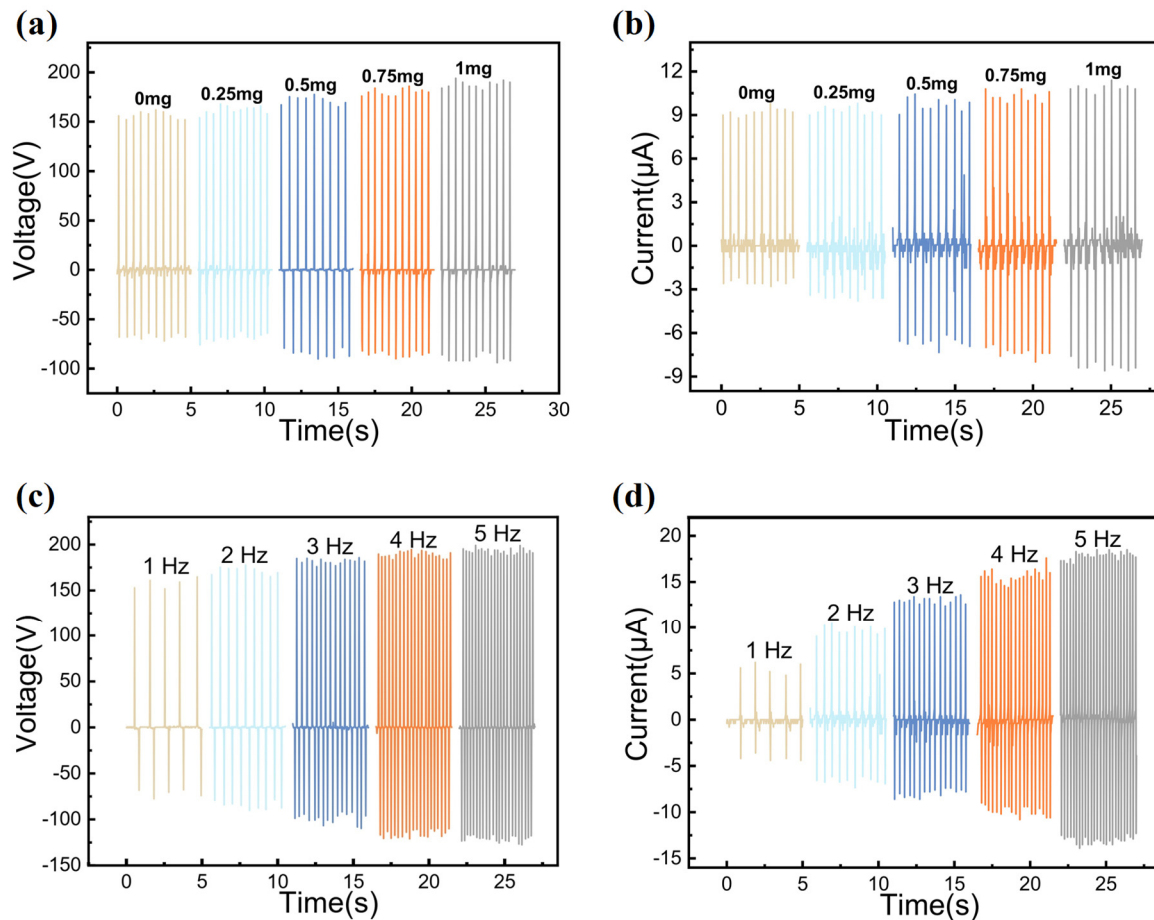

Figure 5. (a) Open-circuit voltage and **(b)** Short-circuit current diagrams of the SF/graphene-PTFE TENG with different concentration of rGO; **(c)** Open-circuit voltage and **(d)** Short-circuit current diagrams of SF/graphene-PTFE TENG at different frequencies.

To provide a systematic overview of optimizing TENG performance with respect to various conditions, a comprehensive comparison of key metrics, including peak-to-peak open-circuit voltage and short-circuit current across all tested configurations, is summarized in Supplementary Materials Table S1.

2.4. The Application of SF/Graphene-PTFE TENG in Keyboard Digital Recognition

As a text input tool for human-computer interaction, the keyboard's accuracy and response speed are critical to the writing experience. TENGs, with their multifaceted advantageous properties, offer a novel and effective technological approach for improving the numeric keypad interface. Human skin occupies a relatively high position in the triboelectric series with a tendency to lose electrons. Due to the work function difference between human skin and SF, friction between the finger and the composite film surface results in charge generation and exchange, thereby producing a stable electrical signal. In this study, a TENG-based sensor array was implemented for the numeric keypad, where electrical signals are generated through contact electrification between the finger and the keys. To ensure the biocompatibility of the SF/graphene composite film during use, the structure of the TENG was modified by removing the original PTFE dielectric layer. This allows the participant's finger to directly

press on the surface of the SF/graphene composite film, simplifying the generator's architecture and switching its operational mode to a single-electrode configuration.

Figure 6a shows the schematic diagram of the digital recognition system. The system consists of a nine-grid self-powered sensor array, an Arduino circuit board for data acquisition, using MATLAB for data analysis and simulation. The sensor is based on high-performance SF film integrated into a single-electrode TENG panel. When finger gestures change on the panel, the corresponding TENG responds to the pressing actions. In this system, nine TENGs were fabricated, each in single-electrode mode and arranged in a nine-grid pattern on a transparent acrylic panel (Figure S7a). The electrodes were connected to wires, which were then linked to a breadboard (Figure S7b). Two resistors (1 kΩ and 10 kΩ) were placed in series to protect the serial port from voltage surges. Voltage data were collected via Arduino pins A0–A8 and transmitted to a computer, allowing real-time plotting of voltage waveforms for up to eight channels.

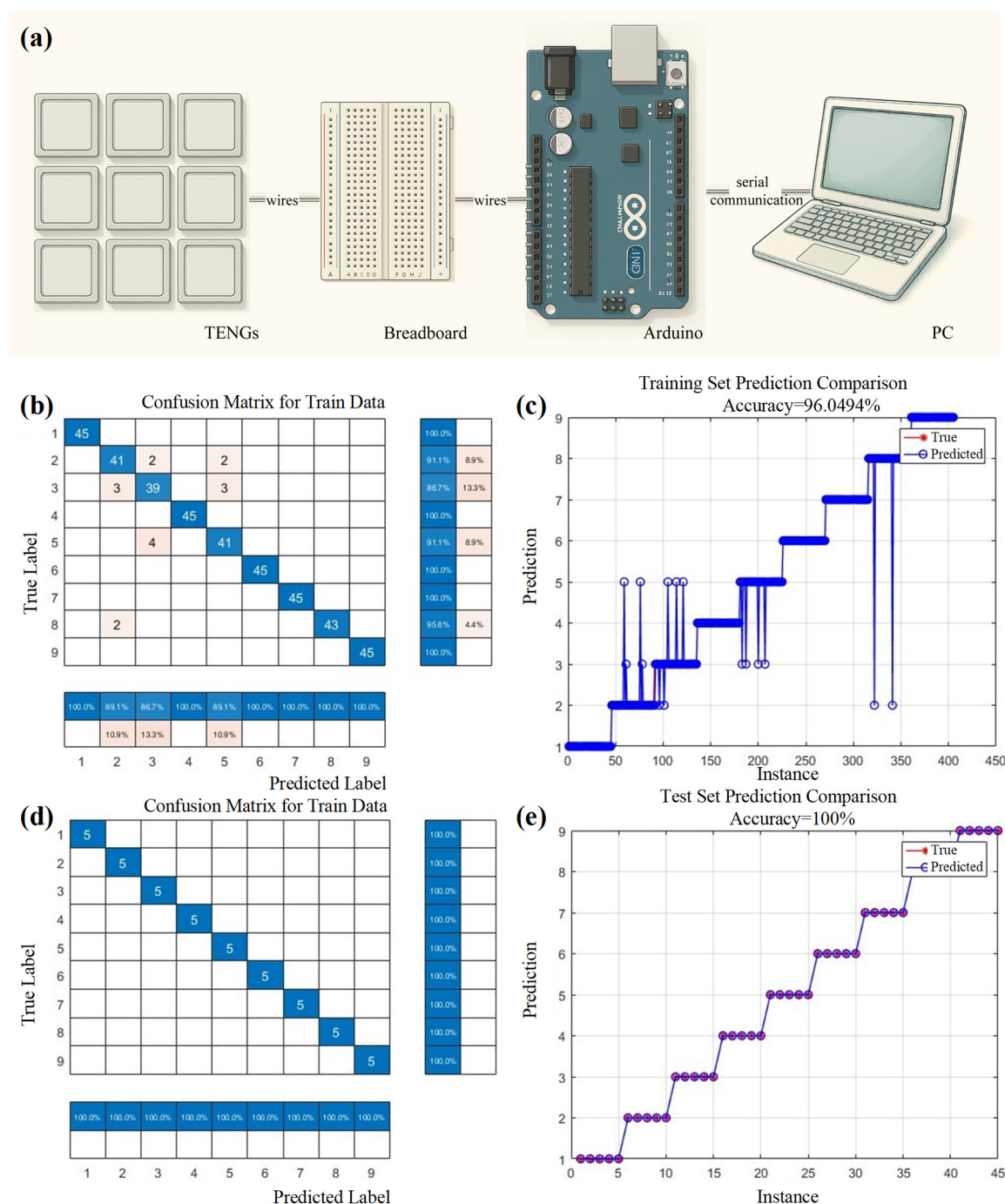**Figure 6.** (**a**) Schematic diagram of the digital recognition system; (**b**) Confusion matrix for 45 training samples; (**c**) Training set prediction results; (**d**) Confusion matrix for 5 test samples; (**e**) Test set prediction results.

In this study, Arduino data acquisition was set at a baud rate of 9600 bits/s with a 100 ms sampling interval, resulting in a sampling frequency of 0.1 s^{-1}. Training data representing digits 1–9 were collected through simulations by two volunteers. The TENGs generated voltage signals ranging from 1.5 V to 15 V, with inactive channels typically below 1.5 V due to noise. MATLAB, integrated with the MATLAB Arduino Support Package, facilitated real-time data processing and display via an Arduino Mega2560 board, as shown in Figure S8. Stronger signals from actuated channels were used to establish threshold-based decision criteria, incorporating peak filtering and error sequence detection. To address potential issues like missed peaks or unrecognized digits, machine learning approaches were applied to enhance system performance, improving digital recognition accuracy.

Libsvm, developed by Professor Zhiren Lin's team at National Taiwan University, was selected for its efficiency and user-friendliness in implementing Support Vector Machines (SVMs), representing one of the most widely used open-source machine learning libraries. Within the MATLAB environment, Libsvm provides comprehensive interfaces supporting model training, parameter selection, cross-validation, and prediction processes. Due to the 8-channel limitation of Arduino's native data acquisition, Parallax Data Acquisition (PLX-DAQ) was employed to simultaneously record all 9 channels and automatically log voltage data into Excel spreadsheets, significantly improving processing efficiency and accuracy. A total of 450 samples (50 per digit) were collected, with 405 allocated for training and 45 for testing.

During MATLAB data processing, feature extraction was performed using a peak detection threshold of 1 V, with a minimum 5-point interval enforced between consecutive peaks within the same channel to prevent redundant signal identification. The complete feature vector was constructed by enumerating peak counts per channel, sequencing active channels, and padding inactive ones. Following randomized dataset partitioning and normalization, SVM parameters including penalty factor (C) and radial basis function parameter (γ) were optimized. The penalty factor C serves as a regularization parameter balancing model complexity against training accuracy, while γ determines the data distribution in feature space and influences support vector selection. Through 5-fold cross-validation, optimal values of C = 11.3137 and γ = 1.007 were identified, yielding 96.05% training accuracy and 100% test accuracy as demonstrated in the confusion matrices (Figure 6b–e). These results not only confirm the model's learning stability and exceptional generalization capability but also highlight its precise predictive performance, indicating high reliability for practical implementations.

3. Conclusions

This study presents a synergistic strategy combining surface microstructuring and graphene doping to significantly enhance the performance of silk fibroin-based triboelectric nanogenerators (TENGs), effectively addressing the critical challenge of balancing high electrical output with material biocompatibility and fabrication simplicity. Finite-element simulations revealed that micro-arch structures effectively concentrate electric fields at sharp features, thereby amplifying charge transfer during contact-separation cycles. Experimentally, the arch-microstructured device achieved a peak-to-peak open-circuit voltage of 224 V, representing a sixfold increase over its flat counterpart. Subsequent doping with reduced graphene oxide (rGO) further improved charge transport, which elevated the peak-to-peak open-circuit voltage to 288 V and short-circuit current to 20 μA, corresponding to additional improvements of 28.57% and 56.99%, respectively. This combined strategy concurrently enhanced mechanical flexibility while preserving the material's biodegradability and operational stability. The practical relevance of this optimized TENG was validated through its integration into a self-powered digital recognition system, which achieved a high classification accuracy of 96.05%. Thus, by establishing a bridge between sustainable biomaterials and functional electronics, this work outlines an effective pathway to advance high-performance, eco-friendly energy harvesters through a novel and scalable methodology, demonstrating broad potential for next-generation self-powered systems.

4. Materials and Methods

4.1. Materials

Natural silk was supplied by Hangzhou Meiyuan Silk Culture Co., Ltd. (Hangzhou, China) The chemical reagents used, including sodium carbonate (Na_2CO_3) and lithium bromide (LiBr), were of analytical grade and procured from China National Medicines Group. 1,4-Butanediol diglycidyl ether was obtained from Aladdin Biochemical Technology Co., Ltd. (Shanghai, China). Dialysis tubing with a molecular weight cutoff (MWCO) of 3500 was purchased from Beijing Lanjieke Technology Co., Ltd. (Beijing, China). Additionally, acrylic plates and PTFE sheets were provided by Dongguan Tongsheng Plastic Materials Co., Ltd. (Dongguan, China) and Taizhou Chenguang Plastic Industry Co., Ltd. (Taizhou, China), respectively.

4.2. Preparation of SF Films

The initial step requires the removal of sericin, a natural adhesive protein that binds silk fibers together. This degumming process enables the extraction of pure fibroin for solution preparation. Sericin, a glue-like protein, coats fibroin strands and maintains structural integrity [41]. In the present study, sodium carbonate solution was employed for degumming due to its effectiveness in breaking down sericin. When sodium carbonate attaches to sericin, the protein's chemical structure is altered, enhancing solubility. Simultaneously, sodium ions facilitate water absorption into sericin, causing swelling and accelerating dissolution [51].

For the degumming procedure, a 0.02 M sodium carbonate solution was prepared by dissolving the powder in 12 L of near-boiling deionized water. Raw silk of 60 g was immersed in the boiling solution for 30 min with periodic stirring. Following extraction, the degummed silk was thoroughly washed with deionized water through four cycles of vigorous kneading to ensure complete sericin removal. Excess water was subsequently squeezed out, and the fibroin was left to dry overnight under ventilation. The fibroin solution was prepared by dissolving 1.35 g of dried fibroin in 5 mL of 9.3 M lithium bromide solution at 60 °C for 3 h. Complete dissolution was followed by dialysis using a 3500 molecular weight cutoff membrane against cold deionized water for 1 h. After adding 300 μL of 1,4-butanediol diglycidyl ether (BDDE) and thorough mixing, the solution was transferred to a mold and heated at 60 °C for 4–5 h [7,52].

4.3. Graphene Doping of SF Films

Considering the complexity of rGO preparation protocols, the established oxidation-reduction method was selected to fabricate SF/graphene composite films, ensuring reproducibility and scalability for industrial-scale production of TENGs. Based on the SF preparation protocol, 0.25 mL of a 2 mg/mL graphene oxide dispersion was incorporated per 1.35 g of dissolved SF solution (prior to curing). The mixture underwent homogenization through ultrasonication at 80 Hz for 1 h. Ascorbic acid ($C_6H_8O_6$), a biologically ubiquitous compound containing a dienediol structure and lactone ring with two chiral carbon centers, demonstrates strong reducibility due to its enediol group. This functional group readily oxidizes to a diketone moiety, forming dehydroascorbic acid. When reacting with graphene oxide, ascorbic acid effectively eliminates oxygen-containing functional groups through ambient-temperature reduction, thereby restoring the material's conductive properties. Accordingly, 20 mg of ascorbic acid was introduced into the graphene oxide dispersion under continuous magnetic stirring for 2 h to obtain the rGO solution. The reduced graphene oxide solution was subsequently blended with dialyzed SF solution and mixed for 12 h. Following the addition of BDDE, the composite solution was thermally cured at 60 °C for 3 h to yield the final SF/graphene composite film.

4.4. Preparation of Surface Microstructures

To explore the influence of surface microstructure on the performance of TENG, two structures, micro-pyramid and micro-arch, were selected for comparison and selection among different structures. Furthermore, for the same structure, different structural densities are used to select the optimal structural density, thereby obtaining the best structure within the feasible range of using molds for production.

To fabricate SF films with micro-pyramid surface microstructures for electrode applications, a series of customized molds were designed. The mold configuration features an overall dimension of 52 mm × 52 mm, with a central coating area of 50 mm × 50 mm specifically designated for film formation. Chamfered edges were incorporated into the design to facilitate subsequent demolding processes. Regarding surface microstructure specifications, each micro-pyramid unit exhibits an area of 1 mm × 1 mm with a consistent depth of 0.5 mm. For comprehensive analysis, curing molds were engineered with regular micro-pyramid arrays corresponding to surface densities ranging from 4 to 25 units per square centimeter, as illustrated in Figure S9a. The dialyzed SF solution was mixed with 300 μL of BDDE and homogenized. The mixture was subsequently transferred into demolding agent-coated molds containing micro-pyramid architectures with varying structural densities. After ensuring uniform solution distribution across the mold surface, the assembly was subjected to thermal stabilization at 60 °C for 5 h to facilitate gelation.

Similarly, to fabricate silk protein films with arch-shaped surface microstructures, a series of customized molds were designed and manufactured. The operations are all the same as the steps of the micro-pyramid structure mentioned above. The molds feature a 52 × 52 mm² base dimension with a 50 × 50 mm² central coating area with arch density ranging from 4 to 25 units per square centimeter, incorporating chamfered edges to facilitate demolding processes. Each unit cell of the arch-shaped microstructure measures a diameter of 1 mm in projected area with a depth of 0.5 mm, as illustrated in Figure S9b.

4.5. Assembly of SF-PTFE and SF/Graphene-PTFE TENGs

The TENG designed in this thesis operates in a vertical contact-separation mode, with SF as the positive triboelectric material and PTFE as the negative triboelectric material. Aluminum foil, serving as the electrode material, is positioned on the backside of the triboelectric materials without direct contact with the friction surface. Aluminum foil was chosen as the electrode material for its function in connecting external circuits and balancing the potential difference generated by the triboelectric materials after electrification. Compared to other common electrode materials such as metals and Indium Tin Oxide (ITO), aluminum or copper foils exhibit superior conductivity, stable physicochemical properties, low cost, and ease of processing. The SF and PTFE layers were cut to dimensions of 3×3 cm^2 and firmly adhered to aluminum foil of the same size. The SF/graphene-PTFE TENG was assembled using the same procedure.

4.6. Establishment of Testing Platform

The electrical output performance testing platform for the TENG includes a digital oscilloscope (TBS 1102b, Tektronix, Inc., Beaverton, OR, USA) with a 100 MΩ probe and a Keithley 6514 electrometer. For electrical signal testing, the Keithley 6514 (Keithley Instruments, Inc., OH, USA) is suitable for ultra-high resistance or ultra-low current measurements, with a sensitivity range of 1 fA, fully covering the short-circuit current of the TENG from milliamperes to nanoamperes. The internal impedance of the TENG is in the megaohm range, and the Tektronix oscilloscope's input impedance of 100 MΩ, combined with its fast response time, allows for accurate acquisition of high-voltage signals at the output, ensuring measurements close to the true values. The output voltage and current were collected by the Tektronix oscilloscope and Keithley 6514 electrometer, respectively, with the open-circuit voltage and short-circuit current sampling rate set to 50 s^{-1}. The three probes from the Keithley 6514 electrometer's input port measured the short-circuit current of the TENG, with the analog and common ports connected to the Tektronix oscilloscope's channel 2, displaying real-time variable fluctuations and trends. Together with the voltage test channel 1 on the Tektronix oscilloscope, the testing circuit was formed. The Tektronix 1102B digital storage oscilloscope features standard functions such as automatic measurement, data logging, frequency counter, and trend graphs. Voltage and current data were saved from the oscilloscope's USB port and visualized using Origin.

Supplementary Materials

The additional data and information can be downloaded at: https://media.sciltp.com/articles/others/25122614 28409771/LDM-25110040-Supplementary-Materials.pdf. Figure S1: (**a**) SEM image of the surface of SF film; (**b**) SEM image of the cross-section of the SF film; (**c**) SEM image of the cross-section of the SF/graphene composite film. Figure S2: (**a**–**f**) Degradation test of silk fibroin/graphene composite films using deionized water for 63 days. Figure S3: Electric potential distribution of the SF-PTFE TENG without microstructure obtained from simulation. Figure S4: The maximum electric potential of TENG with different structures during (**a**) Separation and (**b**) Contact. Figure S5: Comparison bar diagram of maximum peak-to-peak open-circuit voltage and short-circuit current for different microstructures with the density of 25 units/cm^2. Figure S6: (**a**) Durability test of SF-PTFE TENG at a frequency of 2 Hz for 400 s; (**b**) Durability test of SF/graphene-PTFE TENG with a concentration of 0.5 mg at a frequency of 2 Hz for 400 s. Figure S7: (**a**) Photograph of nine-grid format TENG recognition device; (**b**) Circuit diagram of the device connected to Arduino Mega2560. Figure S8: (**a**–**i**) Identification of device voltages for numbers 1 to 9. Figure S9: (**a**) Uniform array of micro-pyramid structures with different densities of silk protein films; (**b**) Uniform array of micro-arch structures with different densities of silk protein films. Table S1: Comprehensive comparison of TENG output performance under different optimization conditions. References [53–56] are cited in supplementary materials.

Author Contributions

B.Z.: writing—original draft preparation, data curation, software, visualization; S.Z.: methodology, validation, visualization; A.H.: investigation, writing—reviewing and editing; X.L.: conceptualization, supervision, writing—reviewing and editing; T.H.: supervision, writing—reviewing and editing; Z.N.: supervision, writing—reviewing and editing; Q.F.: investigation; M.S.: investigation; All authors have read and agreed to the published version of the manuscript.

Institutional Review Board Statement

Not applicable.

Informed Consent Statement

Not applicable.

Data Availability Statement

Data in this work have been presented in the manuscript. If necessary, please contact the corresponding author for more information.

Conflicts of Interest

The authors declare no conflict of interest.

Use of AI and AI-Assisted Technologies

No AI tools were utilized for this paper.

References

1. Chen, H.; Wang, J.; Ning, A. Optimization of a Rolling Triboelectric Nanogenerator Based on the Nano-Micro Structure for Ocean Environmental Monitoring. *ACS Omega* **2021**, *6*, 21059–21065.
2. Wang, Z.L.; Wu, W. Nanotechnology-Enabled Energy Harvesting for Self-Powered Micro-/Nanosystems. *Angew. Chem. Int. Ed.* **2012**, *51*, 11700–11721.
3. Wang, Z.L. Triboelectric Nanogenerators as New Energy Technology for Self-Powered Systems and as Active Mechanical and Chemical Sensors. *ACS Nano* **2013**, *7*, 9533–9557.
4. Wang, Z.L. Triboelectric Nanogenerators as New Energy Technology and Self-Powered Sensors-Principles, Problems and Perspectives. *Faraday Discuss.* **2014**, *176*, 447–458.
5. Khandelwal, G.; Maria Joseph Raj, N.P.; Kim, S.J. Materials Beyond Conventional Triboelectric Series for Fabrication and Applications of Triboelectric Nanogenerators. *Adv. Energy Mater.* **2021**, *11*, 2101170.
6. Tao, X.; Chen, X.; Wang, Z.L. Design and Synthesis of Triboelectric Polymers for High Performance Triboelectric Nanogenerators. *Energy Environ. Sci.* **2023**, *16*, 3654–3678.
7. Li, X.; Hu, N.; Fan, Q.; et al. High-Performance Triboelectric Nanogenerator Based on Natural Silk Fibroin and Microstructured Polytetrafluoroethylene for Self-Powered Electronics and Wearable Sensing. *Mater. Today Commun.* **2024**, *38*, 108418.
8. Zhang, H.; Zhang, D.Z; Wang, D.Y.; et al. Flexible Single-Electrode Triboelectric Nanogenerator with MWCNT/PDMS Composite Film for Environmental Energy Harvesting and Human Motion Monitoring. *Rare Met.* **2022**, *41*, 3117–3128.
9. Cheng, G.G.; Jiang, S.Y.; Li, K.; et al. Effect of Argon Plasma Treatment on the Output Performance of Triboelectric Nanogenerator. *Appl. Surf. Sci.* **2017**, *412*, 350–356.
10. Sutka, A.; Ruza, J.; Jarvekulg, M.; et al. Triboelectric Nanogenerator Based on Immersion Precipitation Derived Highly Porous Ethyl Cellulose. *J. Electrostat.* **2018**, *92*, 1–5.
11. Wen, D.L.; Sun, D.H.; Huang, P.; et al. Recent Progress in Silk Fibroin-Based Flexible Electronics. *Microsyst. Nanoeng.* **2021**, *7*, 35.
12. Gulahmadov, O.; Muradov, M.B.; Mamedov, H.; et al. Enhancement of Triboelectric Nanogenerators with Nylon/TiO$_2$ Nanocomposite Films. *MRS Commun.* **2024**, *14*, 114–120.
13. Fan, F.R.; Lin, L.; Zhu, G.; et al. Transparent Triboelectric Nanogenerators and Self-Powered Pressure Sensors Based on Micropatterned Plastic Films. *Nano Lett.* **2012**, *12*, 3109–3114.
14. Kim, J.; Gulahmadov, O.; et al. Enhancement of Performance of Triboelectric Generators by Introduction of Micro- and Nano-Structures on Triboelectric Films. *J. Mater. Sci. Mater. Electron.* **2021**, *32*, 24661–24680.
15. Xi, Y.; Zhang, F.; Shi, Y. Effects of Surface Micro-Structures on Capacitances of the Dielectric Layer in Triboelectric Nanogenerator: A Numerical Simulation Study. *Nano Energy* **2021**, *79*, 105432.

16. Zou, Y.; Xu, J.; Chen, K.; et al. Advances in Nanostructures for High-Performance Triboelectric Nanogenerators. *Adv. Mater. Technol.* **2021**, *6*, 2000919.

17. Kim, D.; Tcho, I.W.; Jin, I.K.; et al. Direct-Laser-Patterned Friction Layer for the Output Enhancement of a Triboelectric Nanogenerator. *Nano Energy* **2017**, *35*, 379–386.

18. Huang, J.; Fu, X.; Liu, G.; et al. Micro/Nano-Structures-Enhanced Triboelectric Nanogenerators by Femtosecond Laser Direct Writing. *Nano Energy* **2019**, *62*, 638–644.

19. Fatemeh, M.; Fathallah, K.; Mahshid, K. Rational Micro/Nano-Structuring for High-Performance Triboelectric Nanogenerator. *J. Alloys Compd.* **2023**, *960*, 170693.

20. Patnam, H.; Dudem, B.; Graham, S.A.; et al. High-Performance and Robust Triboelectric Nanogenerators Based on Optimal Microstructured Poly(Vinyl Alcohol) and Poly(Vinylidene Fluoride) Polymers for Self-Powered Electronic Applications. *Energy* **2021**, *223*, 120031.

21. Mule, A.R.; Dudem, B.; Yu, J.S. High-Performance and Cost-Effective Triboelectric Nanogenerators by Sandpaper-Assisted Micropatterned Polytetrafluoroethylene. *Energy* **2018**, *165*, 677–684.

22. Dudem, B.; Dharmasena, R.D.I.G.; Graham, S.A.; et al. Exploring the Theoretical and Experimental Optimization of High-Performance Triboelectric Nanogenerators Using Microarchitectured Silk Cocoon Films. *Nano Energy* **2020**, *74*, 104882.

23. Dudem, B.; Heo, J.H.; Leem, J.W.; et al. CH$_3$NH$_3$PbI$_3$ Planar Perovskite Solar Cells with Antireflection and Self-Cleaning Function Layers. *J. Mater. Chem. A* **2016**, *4*, 7573–7579.

24. Dudem, B.; Kim, D.H.; Mule, A.R.; et al. Enhanced Performance of Microarchitectured PTFE-Based Triboelectric Nanogenerator via Simple Thermal Imprinting Lithography for Self-Powered Electronics. *ACS Appl. Mater. Interfaces* **2018**, *10*, 24181–24192.

25. Liu, Y.; Ping, J.; Ying, Y.; et al. Recent Progress in 2D-Nanomaterial-Based Triboelectric Nanogenerators. *Adv. Funct. Mater.* **2021**, *31*, 2009994.

26. Lan, L.; Yin, T.; Jiang, C.; et al. Highly Conductive 1D-2D Composite Film for Skin-Mountable Strain Sensor and Stretchable Triboelectric Nanogenerator. *Nano Energy* **2019**, *62*, 319–328.

27. Nuthalapati, S.; et al. Wearable High-Performance MWCNTs/PDMS Nanocomposite-Based Triboelectric Nanogenerators for Haptic Applications. *IEEE J. Flex. Electron.* **2024**, *3*, 393–400.

28. Biswas, M.; Bhattacharya, D.; Mondal, R.; et al. Surface Engineered MoS$_2$-Based Novel Vertical Triboelectric Nanogenerator (V-TENG) for Wireless Information Processing. *Small* **2025**, *21*, 2410608.

29. Zhai, L.; Cui, S.; Tong, B.; et al. Bromine-Functionalized Covalent Organic Frameworks for Efficient Triboelectric Nanogenerator. *Chem. Eur. J.* **2020**, *26*, 5784–5788.

30. Khandelwal, G.; Chandrasekhar, A.; Raj, N.P.M.J.; et al. Metal-Organic Framework: A Novel Material for Triboelectric Nanogenerator-Based Self-Powered Sensors and Systems. *Adv. Energy Mater.* **2019**, *9*, 1803581.

31. Bhatta, T.; Maharjan, P.; Cho, H.; et al. High-Performance Triboelectric Nanogenerator Based on MXene Functionalized Polyvinylidene Fluoride Composite Nanofibers. *Nano Energy* **2021**, *81*, 105670.

32. Yan, J.; Wang, H.; Wang, X.; et al. High-Performance Triboelectric Nanogenerators with Laser-Induced Graphene Pattern for Efficient Charge Transfer. *Appl. Surf. Sci.* **2024**, *661*, 160034.

33. Wu, Y.; Luo, Y.; Qu, J.; et al. Liquid Single-Electrode Triboelectric Nanogenerator Based on Graphene Oxide Dispersion for Wearable Electronics. *Nano Energy* **2019**, *64*, 103948.

34. Gulahmadov, O.; Gahramanli, L.; Muradov, M.; et al. Optimization of MWCNT Concentration in Nylon-Based Nanocomposites for Enhanced Nanogenerator Performance. *J. Mater. Sci. Mater. Electron.* **2025**, *20*, 101.

35. Parmar, S.; Biswas, A.; Singh, S.K.; et al. Coexisting 1T/2H Polymorphs, Reentrant Resistivity Behavior, and Charge Distribution in MoS$_2$-hBN 2D/2D Composite Thin Films. *Phys. Rev. Mater.* **2019**, *3*, 074007.

36. Jeong, Y.R.; Oh, S.Y.; Kim, J.W.; et al. A Highly Conductive and Electromechanically Self-Healable Gold Nanosheet Electrode for Stretchable Electronics. *Chem. Eng. J.* **2020**, *384*, 123336.

37. Li, W.; Zhang, Y.; Liu, L.; et al. A High Energy Output Nanogenerator Based on Reduced Graphene Oxide. *Nanoscale* **2015**, *7*, 18147–18151.

38. Morala-Martinez, C.L.; Rodriguez-Ortega, A.; Rodriguez, N.; et al. Biofabrication of Silk Fibers with Enhanced Conductivity through Silkworm Feeding with Reduced Graphene Oxide: Implications for Smart Textile Innovations. *ACS Appl. Nano Mater.* **2024**, *7*, 6229–6241.

39. Inagaki, M.; Kim, Y.A.; Endo, M. Graphene: Preparation and Structural Perfection. *J. Mater. Chem.* **2011**, *21*, 3280–3294.

40. Novoselov, K.S.; Falko, V.I.; Colombo, L.; et al. A Roadmap for Graphene. *Nature* **2012**, *490*, 192–200.

41. Low, J.T.; Yusoff, N.; Othman, N.; et al. Silk Fibroin-Based Films in Food Packaging Applications: A Review. *Compr. Rev. Food Sci. Food Saf.* **2022**, *21*, 2253–2273.

42. Lu, Q.; Hu, X.; Wang, X.; et al. Water-Insoluble Silk Films with Silk I Structure. *Acta Biomater.* **2010**, *6*, 1380–1387.

43. Nguyen, V.T.; Le, H.D.; Nguyen, V.C.; et al. Synthesis of Multi-Layer Graphene Films on Copper Tape by Atmospheric Pressure Chemical Vapor Deposition Method. *Adv. Nat. Sci. Nanosci. Nanotechnol.* **2013**, *4*, 035012.

44. Liu, C.; Li, J.; Che, L.; et al. Toward Large-Scale Fabrication of Triboelectric Nanogenerator (TENG) with Silk-Fibroin Patches Film via Spray-Coating Process. *Nano Energy* **2017**, *41*, 359–366.

45. Li, Z.; Xu, S.; Xu, Z.; et al. Enhancing Cellular Behavior in Repaired Tissue via Silk Fibroin-Integrated Triboelectric Nanogenerators. *Microsyst. Nanoeng.* **2024**, *10*, 68.

46. Suo, X.; Li, B.; Ji, H.; et al. Dielectric Layer Doping for Enhanced Triboelectric Nanogenerators. *Nano Energy* **2023**, *114*, 108651.

47. Huang, Y.J.; Ke, K.H.; Chung, C.K. Effect of Commercial P25 TiO_2 Doping in Polydimethylsiloxane Tribo-Film on the Output Performance of Triboelectric Nanogenerator and Its Application. *Surf. Coat. Technol.* **2024**, *482*, 130721.

48. Li, Z.; Wang, X.; Hu, Y.; et al. Triboelectric Properties of $BaTiO_3$/Polyimide Nanocomposite Film. *Appl. Surf. Sci.* **2022**, *572*, 151391.

49. Jung, H.; Ouro-Koura, H.; Salalila, A.; et al. Frequency-Multiplied Cylindrical Triboelectric Nanogenerator for Harvesting Low Frequency Wave Energy to Power Ocean Observation System. *Nano Energy* **2022**, *99*, 107365.

50. Du, T.; Dong, F.; Xi, Z.; et al. Recent Advances in Mechanical Vibration Energy Harvesters Based on Triboelectric Nanogenerators. *Small* **2023**, *19*, 2300401.

51. Yu, H.; Kong, J.; Mao, M.; et al. Self-Powered Biodegradable and Antibacterial MoS_2-Based Triboelectric Nanogenerators for the Acceleration of Wound Healing in Diabetes. *Nano Energy* **2024**, *121*, 109225.

52. Farokhi, M.; Aleemardani, M.; Solouk, A.; et al. Crosslinking Strategies for Silk Fibroin Hydrogels: Promising Biomedical Materials. *Biomed. Mater.* **2021**, *16*, 022004.

53. Wang, Z.L. On Maxwell's Displacement Current for Energy and Sensors: The Origin of Nanogenerators. *Mater. Today* **2017**, *20*, 74–82.

54. Niu, S.; Wang, S.; Lin, L.; et al. Theoretical Study of Contact-Mode Triboelectric Nanogenerators as an Effective Power Source. *Energy Environ. Sci.* **2013**, *6*, 3576–3583.

55. Niu, S.; Liu, Y.; Chen, X.; et al. Theory of Freestanding Triboelectric-Layer-Based Nanogenerators. *Nano Energy* **2015**, *12*, 760–774.

56. Niu, S.; Liu, Y.; Zhou, Y.S.; et al. Optimization of Triboelectric Nanogenerator Charging Systems for Efficient Energy Harvesting and Storage. *IEEE Trans. Electron Devices* **2015**, *62*, 641–647.